NANO LETTERS

pubs.acs.org/NanoLett Letter

Epitaxial Electrodeposition of Zinc on Different Single Crystal Copper Substrates for High Performance Aqueous Batteries

Xin Xiao, Louisa C. Greenburg, Yuqi Li, Menghao Yang, Yan-Kai Tzeng, Chenxi Sui, Yucan Peng, Yecun Wu, Zewen Zhang, Xin Gao, Rong Xu, Yusheng Ye, Pu Zhang, Yufei Yang, Arturas Vailionis, Po-chun Hsu, Jian Qin, and Yi Cui*

Cite This: *Nano Lett.* 2025, 25, 1305−1313 **Read Online**

ABSTRACT: The aqueous zinc metal battery holds great potential for large-scale energy storage due to its safety, low cost, and high theoretical capacity. However, challenges such as corrosion and dendritic growth necessitate controlled zinc deposition. This study employs epitaxy to achieve large-area, dense, and ultraflat zinc plating on textured copper foil. High-quality copper foils with Cu(100), Cu(110), and Cu(111) facets were prepared and systematically compared. The results show that Cu(111) is the most favorable for zinc deposition, offering the lowest nucleation overpotential, diffusion energy, and interfacial energy with a Coulombic efficiency (CE) of 99.93%. The study sets a record for flat-zinc areal loading at 20 mAh/cm^2. These findings provide some clarity on the best-performing copper and zinc crystalline facets, with Cu(111)/Zn(0002) ranking the highest. Using a MnO_2−Zn full cell model, the research achieved an exceptional cycle life of over 800 cycles in a cathode−anode-free battery configuration.

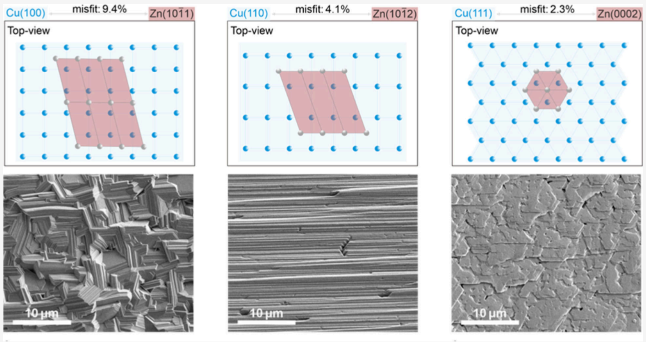

KEYWORDS: *Epitaxial growth, Zinc ion battery, Copper single crystal, EBSD, Pole figure, cathode-anode-free aqueous battery*

The rapid growth of the global energy storage market[1] has driven flourishing research for cost-effective and long-duration batteries. This surge is underpinned by the escalating demand for the integration of renewable energy and enhanced power management systems. Among the various batteries for grid-scale energy storage, the rechargeable aqueous zinc (Zn) metal battery utilizing the plating/stripping electrochemistry between the Zn^{2+} cation and zinc metal stands out as a highly promising anode. This is attributed to its compatibility with nonflammable aqueous electrolyte,[2−6] tolerance to ambient conditions,[4] high gravimetric capacity (820 mAh g^{-1}), 3 times higher volumetric capacity (5854 Ah L^{-1}) than lithium metal,[7] low cost, and high abundance in Earth's crust.[8,9] However, the practical application of rechargeable zinc metal batteries faces critical challenges, particularly due to dendrite formation and corrosion, which impede their energy efficiency and life.

To overcome these challenges in zinc metal anodes, various approaches involving architectural design,[10,11] electrolyte optimization,[12−15] and interfacial engineering[16−19] have been explored. Strategies such as 3D-wire/porous Zn structures have been employed to suppress Zn dendrite growth.[10] Innovations in electrolytes, including various salts (e.g., $Li_2ZnCl_4{\cdot}9H_2O$,[13] $ZnCl_2$,[20] $Zn(ClO_4)_2$,[5] $ZnSO_4$,[6] $Zn(Ac)_2$,[21,22] $Zn(TFSI)_2$,[4,23] $Zn(OTf)_2$[24,25]) and solvents (e.g., propylene carbonate,[23] triethyl phosphate,[24] N,N-dimethylformamide,[26] ethylene glycol,[27] dimethyl sulfoxide[28]), aim to stabilize zinc deposition. Interfacial engineering, using materials like polymers (e.g., polyamide,[29] polyacrylonitrile[30]) and inorganic compounds (e.g., $CaCO_3$,[17] TiO_2,[31] zeolitic imidazolate framework-8[32]), helps regulate zinc-ion flux and prevent corrosion. These methods typically reduce Zn^{2+} mobility to minimize corrosion and dendrite formation, improving dendrite-free zinc plating at low current densities,[18,33] but potentially limiting high-rate capabilities of zinc batteries. In contrast, when using the common low cost 1 M $ZnSO_4$ aqueous electrolyte, dendrite growth increases notably with the reduction of current density, as shown in Figure S1.

An alternative method to preserve Zn^{2+} mobility, without altering electrolyte chemistry, involves epitaxy-controlled metal anode growth, as developed by Zheng et al.[34] This approach uses graphene layers as an epitaxial template for Zn(0002) deposition, with a prediction of Co and Ti as other potential

Received: September 14, 2024
Revised: January 14, 2025
Accepted: January 15, 2025
Published: January 21, 2025

https://doi.org/10.1021/acs.nanolett.4c04535

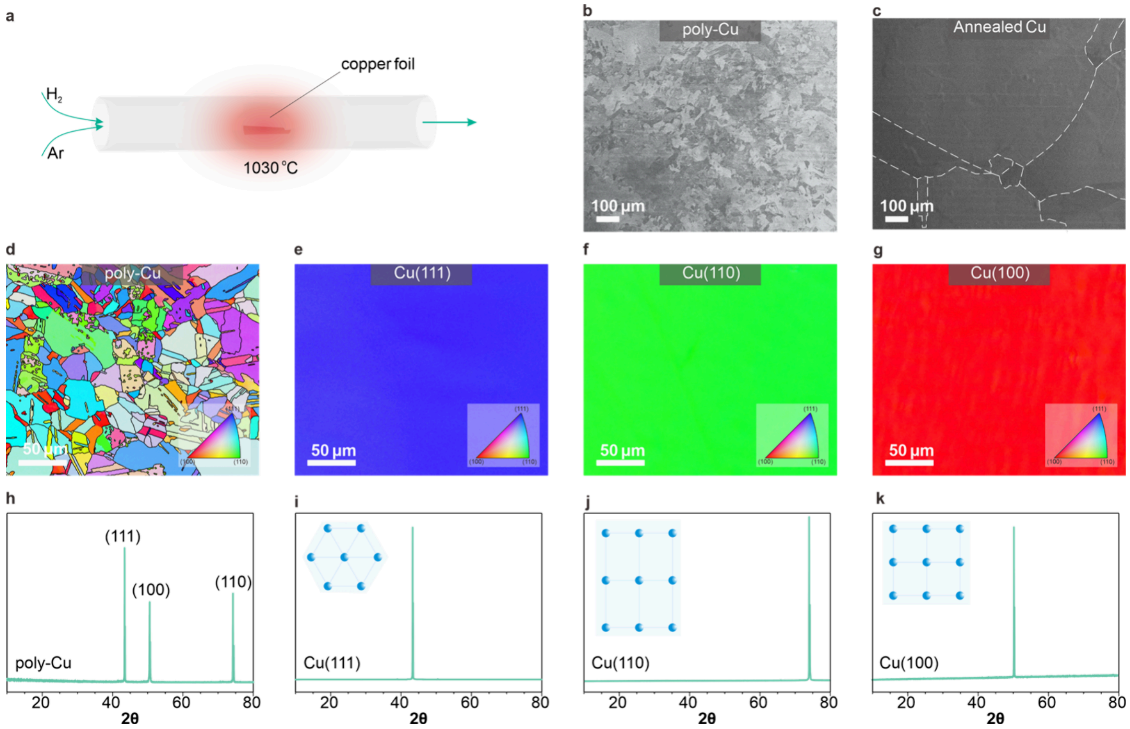

Figure 1. Synthesis of high-quality Cu single crystals through annealing. (a) Illustration of the annealing process of copper foil. (b,c) SEM images of copper foil before (b) and after (c) annealing. (d–k) EBSD mapping and XRD spectra of the poly-Cu (d, h), obtained Cu(111) (e, i), Cu(110) (f, j), and Cu(100) (g, k), respectively. The inner figures in h–k refer to the surface atomic arrangement of the corresponding copper facets.

low-misfit substrates for zinc growth.[34] This technique offers a promising strategy for dendrite-free zinc without compromising the Zn^{2+} kinetics. However, maintaining the epitaxial deposition of Cu on graphene and its good electrochemical performance to practical areal capacities (>10 mAh/cm^2) remains to be demonstrated. In addition, it is not yet clear which facet of zinc would provide the best electrochemical performance. Thus, a high-quality substrate capable of epitaxially growing various zinc facets is crucial for both practical applications and a fundamental understanding. Although various epitaxial substrates (such as copper) for zinc metal batteries have been identified, there remains a debate over which zinc facet and which substrate facet are optimal. Some assert that Zn(0002) is the superior zinc facet,[34,35] while others advocate for Zn(10$\bar{1}$1).[36] Meanwhile, some claim Cu(220)[35,37] is the optimal substrate facet for Zn growth, while others favor Cu(100)[37] or Cu(111).[38−40] This ongoing dispute is likely rooted in the absence of high-quality single-crystal Cu substrates and a systematic understanding of the epitaxial growth processes for various zinc facets.

To address this debate, we synthesized high-quality copper single crystals fully exposed to either Cu(100), Cu(110), or Cu(111) facets. The zinc deposition on three specific copper facets was explored. We find that zinc deposits on single-crystal Cu foil in a compact, highly epitaxial manner, in contrast to its random growth on polycrystalline copper (poly-Cu) foil. Among the facets studied, Cu(111) demonstrated the lowest nucleation overpotential and highest Coulombic efficiency. Density functional theory (DFT) calculations confirmed the lowest zinc diffusion and interfacial energy for Cu(111). The uniform zinc deposition of Zn(0002) on the Cu(111) substrate results in batteries with enhanced corrosion resistance and a significantly longer cycle life in symmetric zinc cells. Moreover, it achieved a record-breaking cycle life in MnO_2−Zn cells with a cathode-anode-free configuration.

High Quality Single Crystal Cu with Different Facets. To produce high-quality Cu facets, an annealing protocol at 1030 °C in a mixed hydrogen−argon atmosphere was used (Figure 1a). By fine-tuning the annealing conditions, we successfully synthesized three common Cu facets (Cu(100), Cu(110), and Cu(111)) as detailed in the methods section. The formation mechanism of Cu(111) during annealing was surface energy governed,[41,42] while an oxygen chemisorption-induced reconstruction mechanism was proposed for Cu(100) and Cu(110) formation.[43] SEM images of postannealing samples reveal larger crystal grains compared to the original small-grained copper foil (poly-Cu; Figure 1b,c). Electron backscatter diffraction (EBSD) mapping, a powerful technique for characterizing grain orientation on the microscopic scale, was used to analyze the surface crystal orientation of copper before and after annealing (Figure 1d–g). In this technique, electrons generated in the SEM are backscattered, causing local diffraction at the sample surface, which is captured as a Kikuchi map by the EBSD detector. These maps were then converted to grain orientations along the *z*-axis using the MTEX method,[44] as shown in Figure 1d–g. It is evident that poly-Cu contains plenty of small crystal grains, while annealed Cu foils all displayed highly uniform orientations of (100), (110), and (111). Statistically, the average grain diameter increased from ~20 μm in poly-Cu to ~4 mm in annealed Cu(111) (Figure S2). X-ray diffraction (XRD) analysis (Figure 1h–k), with a 5 mm × 5 mm irradiation area, reveals sole significant Cu(100), Cu(110), and Cu(111) peaks for annealed copper, confirming the large-area high-quality synthesized single crystal. These high-quality Cu facets provide a robust experimental basis for studying zinc deposition behaviors on different Cu facets.

https://doi.org/10.1021/acs.nanolett.4c04535
Nano Lett. 2025, 25, 1305−1313

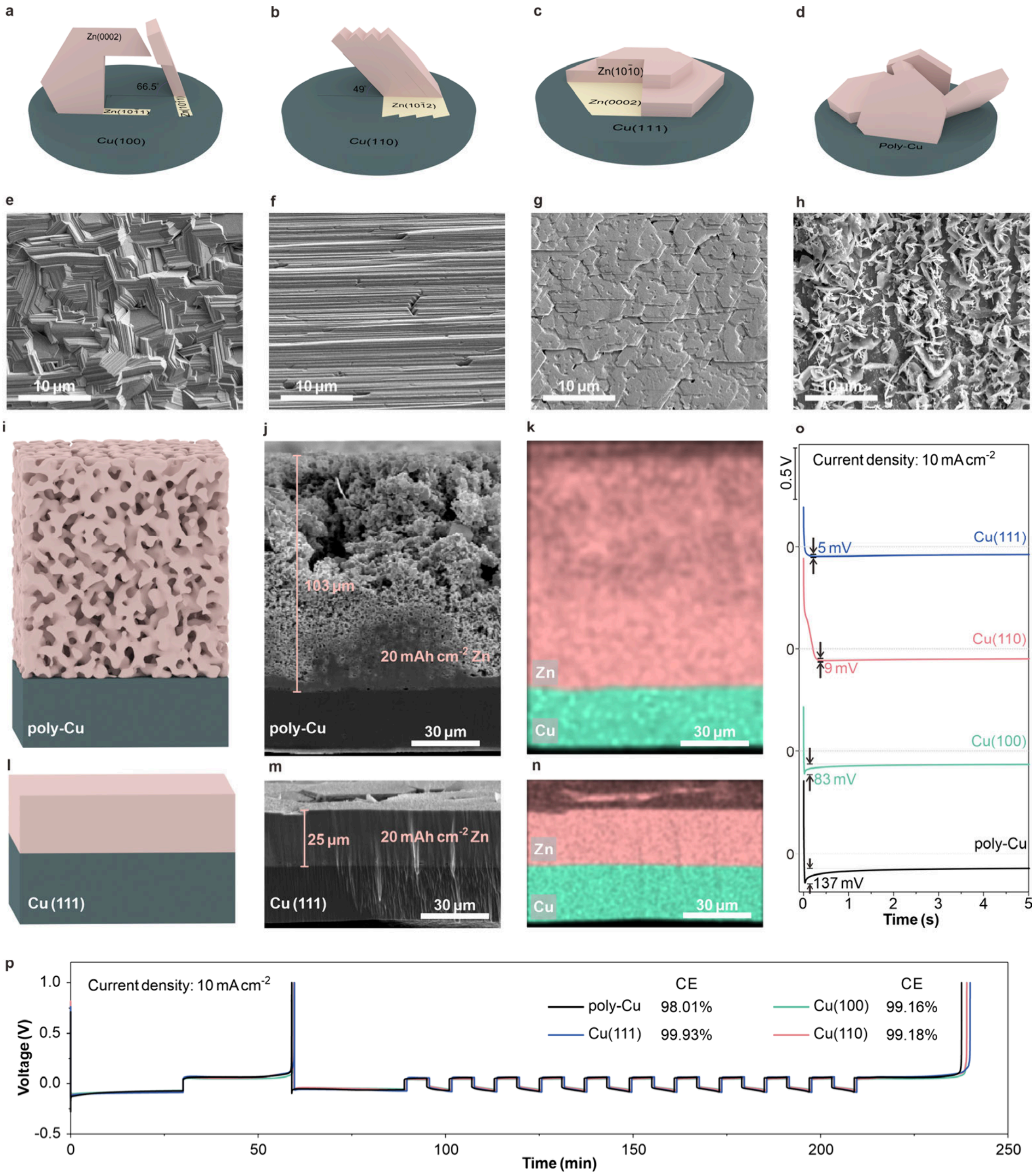

Figure 2. Electrodeposition of zinc onto different textured copper foils. (a−h) Models and SEM images of electrodeposited Zn (1 mAh cm^{-2} @ 10 mA cm^{-2}) onto Cu(100) (a,e), Cu(110) (b,f), Cu(111) (c,g), and poly-Cu (d,h). (i−k) Cross-section model, image, and EDS mapping of high-capacity zinc loading (20 mAh cm^{-2}) onto poly-Cu. (l−n) Cross-section model, image, and EDS mapping of high-capacity zinc loading (20 mAh cm^{-2}) onto Cu(111). (o) Nucleation overpotential of zinc plating on different copper surfaces. (p) Aurbach measurement of zinc plating on different copper surfaces. The calculated diffusion energy barrier of a zinc atom on different Cu facets and detailed information can be found in Figure S5.

Electrodeposition of Zn on poly-Cu and Single Crystal Cu Facets. We examined zinc deposition on various copper foils in 1 M $ZnSO_4$ electrolyte at 10 mA cm^{-2} to an areal capacity of 1 mAh cm^{-2}. As shown in Figure 2a−h, zinc forms random hexagonal shapes on poly-Cu with small disoriented crystals. Upon switching to single-crystal copper foils, zinc deposition becomes compact and textured (Figure 2a−c, e−g). On Cu(100), zinc flakes appear hexagonal and perpendicular to each other yet slanted relative to the foil, resulting in a slightly uneven surface. In contrast, zinc deposition on Cu(110) and Cu(111) results in flat surfaces and a uniform orientation. Specifically, Zn is parallel to Cu(111), while it is uniformly slanted on Cu(110). Additionally, this epitaxy-controlled zinc plating is not limited to $ZnSO_4$ electrolyte, as similar flat zinc plating was also observed in zinc acetate and zinc bis(trifluoromethanesulfonyl)imide electrolyte using Cu(111) (Figure S3).

Such epitaxy control of zinc plating offers a solution for continuous, dendrite-free deposition, making it possible to achieve high areal mass loading in electrodes, which is crucial for enhanced energy density to both cathode[45] and anode[46] materials. Here, benefiting from the large-area high-quality of single crystal copper, we have successfully plated 20 mAh cm^{-2} of dendrite-free zinc onto Cu(111) with just 25 μm thickness

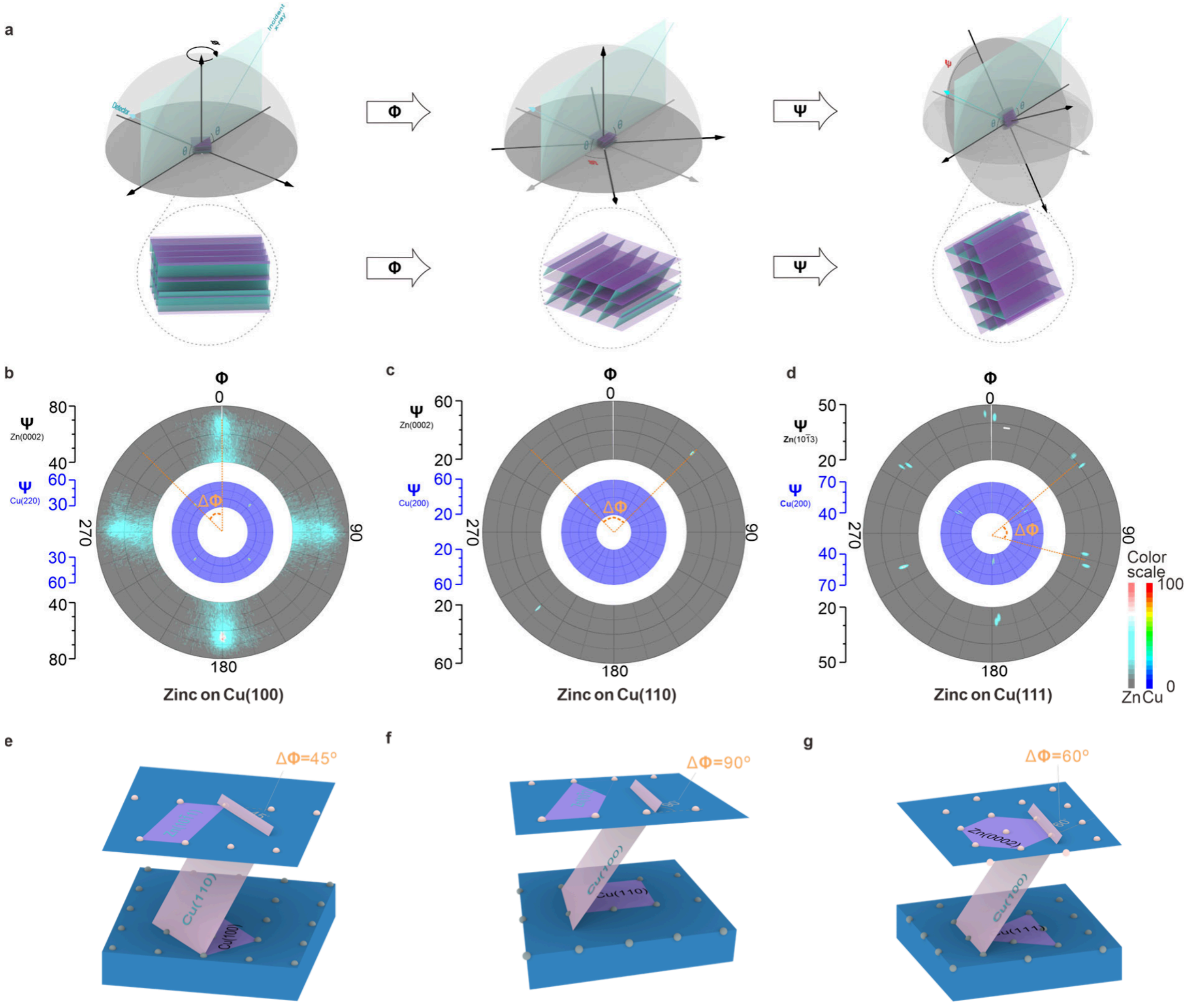

Figure 3. Pole figure illustration of zinc onto different Cu facets. (a) The mechanism of pole figure measurement. In the top part of this figure, the gray hemisphere refers to the sample stage, and the cyan rectangle represents the X-ray-irradiation-pathway plane. In the bottom of this figure, the purple plane is the one that parallels the sample surface (namely a pole), while the blue plane is the reference frame that fulfills Bragg's law at θ, meaning that a significant X-ray signal will be triggered if the blue plane becomes horizontal by reasonable rotating. It is also not difficult to find that Ψ is the angle between the pole plane and the reference plane. (b−d) Pole figures of the 1 mAh cm^{-2} zinc deposited onto Cu(100) (b), Cu(110) (c), and Cu(111) (d), where the circular ring with gray shadow refers to the pole figure of Zn, and the circular ring with blue shadow refers to the pole figure of Cu. (e−g) 3D model illustration of the in-plane angle ($\Delta\Phi$) between epitaxial matched Cu and Zn facets (e, Cu(100)−Zn(10$\bar{1}$1); f, Cu(110)−Zn(10$\bar{1}$2); g, Cu(111)−Zn(0002)). Note that in Figure 3d there are two conjugated points here originating from two large single-crystal Cu(111) grains with a small in-plane angle to each other. More detailed pole figure analysis of zinc on Cu can be found in Figures S9−S11.

(Figure 2i−n), setting a flat-zinc plating capacity record in aqueous electrolytes. In contrast, the zinc thickness on poly-Cu reaches 103 μm at the same capacity (Figure 2i−k). Dense deposition on Cu(111) is confirmed by cross-sectional imaging and EDS mapping, indicating an epitaxy-regulated, zero-porosity plating process, unlike the 65% porosity seen in poly-Cu (Figure S4).

Besides the morphological differences in electrodeposited zinc on various copper foils, their electrochemical performance also differs, as shown by the Aurbach method initially developed for lithium metal.[47−49] The Coulombic efficiency (CE) of Zn plating and stripping on poly-Cu stands at 98.01%, while single-crystal Cu(100), Cu(110), and Cu(111) enable enhanced CEs of 99.16%, 99.18%, and 99.93%, respectively (Figure 2p). This suggests higher reversibility when transitioning from polycrystalline to single-crystal surfaces, with Cu(111) being the most efficient. Similarly, the trend in nucleation overpotentials (poly-Cu > Cu(100) > Cu(110) > Cu(111)) shown in Figure 2o follows the reversibility pattern, suggesting that a higher nucleation overpotential leads to uneven zinc plating, resulting in a more exposed zinc surface that is prone to corrosion side reactions.

To understand the nucleation discrepancies across different copper facets, we propose that the diffusion energy barrier plays a crucial role, especially given the similarity in the Zn^{2+} distribution on flat single-crystal Cu interfaces. Zinc electroplating involves reduction of Zn^{2+} to Zn atoms on the substrate, followed by diffusion to form nuclei (Figure S5). Density functional theory (DFT) calculations show that Cu(111) has the lowest diffusion energy barrier (Figure S5),

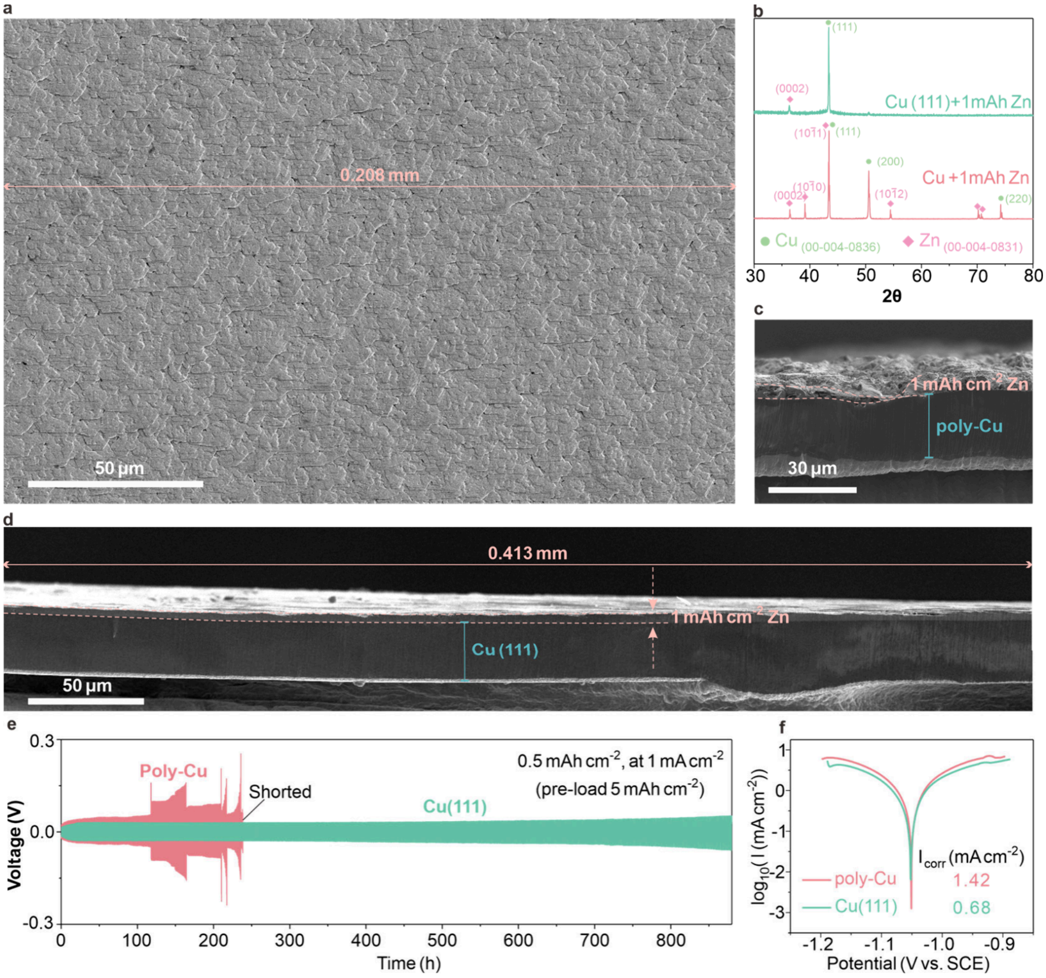

Figure 4. Electrodeposition of zinc onto copper foil. (a) Morphology of deposited Zn onto Cu(111) foil (1 mAh cm^{-2} @ 10 mA cm^{-2}). (b) XRD patterns of deposited Zn onto pristine copper foil and Cu(111) foil. (c) Cross-section images of poly-Cu with 1 mAh cm^{-2} Zn. (d) Cross-section images of Cu(111) with 1 mAh cm^{-2} Zn. (e) Symmetric cell of preloaded 5 mAh cm^{-2} Zn cycling at 0.5 mAh cm^{-2} and 1 mA cm^{-2} (electrolyte: 1 M $ZnSO_4$). (f) Linear polarization curves of the Zn deposited onto poly-Cu and Cu(111) foil in an electrolyte of 1 M $ZnSO_4$.

favoring a uniform zinc layer formation. In-situ optical cell observations (Figure S6 and Video S1 and Video S2) reveal quick zinc diffusion on Cu(111) due to this low energy barrier, unlike the isolated zinc dots on poly-Cu. This could be why Cu(111) excels in compact zinc plating, reversibility, and low nucleation overpotential, making it ideal for rechargeable zinc ion battery applications.

Crystallinity Relationship between Electrodeposited Zinc and Copper. The orientation of electrodeposited zinc onto different Cu facets monitored by XRD (Figure S7) indicates that the preferred orientations of zinc on Cu(100), Cu(110), and Cu(111) are Zn(10$\bar{1}$1), Zn(10$\bar{1}$2), and Zn(0002), respectively. To understand the epitaxial deposition mechanism on different copper facets, we conducted DFT simulations to determine the interfacial energy between various Cu and Zn facets. The main facets of zinc on Cu(100), Cu(110), and Cu(111) are identified as Zn(10$\bar{1}$1), Zn(10$\bar{1}$2), and Zn(0002), respectively, matching well with their low lattice misfits (under 10%) based on XRD spectra (Figure S7). Notably, the Cu(111)/Zn(0002) pair exhibits the least facet misfit, at 2.3%. DFT calculations confirm that these Zn facets are the most thermodynamically favorable for their respective Cu facets (Figure S8d-f), aligning with the presumed epitaxial relationships (Figure 2a-h). This theoretical insight supports the observed epitaxial patterns.

We further employed pole figure analysis to elucidate the epitaxial relationship between Cu and Zn. This method is chosen because it yields statistical data across a substantial sample size and is particularly useful for examining flat samples. In contrast, other analytical techniques like TEM sample only suitable minuscule areas and are difficult to observe with flat, dense samples. Pole figure assessments offer two-dimensional visual depictions of orientation, unlike the one-dimensional spectra obtained from powder X-ray diffraction, thereby illustrating the alignment of a chosen sample plane (the pole) relative to a reference frame (Figure 3a). Correlating Cu and Zn pole figures allows us to determine the relative in-plane angles at Cu−Zn interfaces (Figures S9−S11). For instance, in Figure 3d, the blue shadow represents the pole figure of single-crystal Cu(111) using Cu(100) as a reference plane. Three symmetrically distributed dot groups correspond to Cu(111) due to copper's cubic symmetry, with Ψ values around 54.8° (the angle between Cu(111) and reference plane-Cu(100)) (Figure S11e). The gray shadow features six dot groups, indicating zinc's hexagonal symmetry and representing Zn(0002) with Ψ values around 37.6° (angle between Zn(0002) and reference plane-Zn(10$\bar{1}$3)) (Figure S11d).

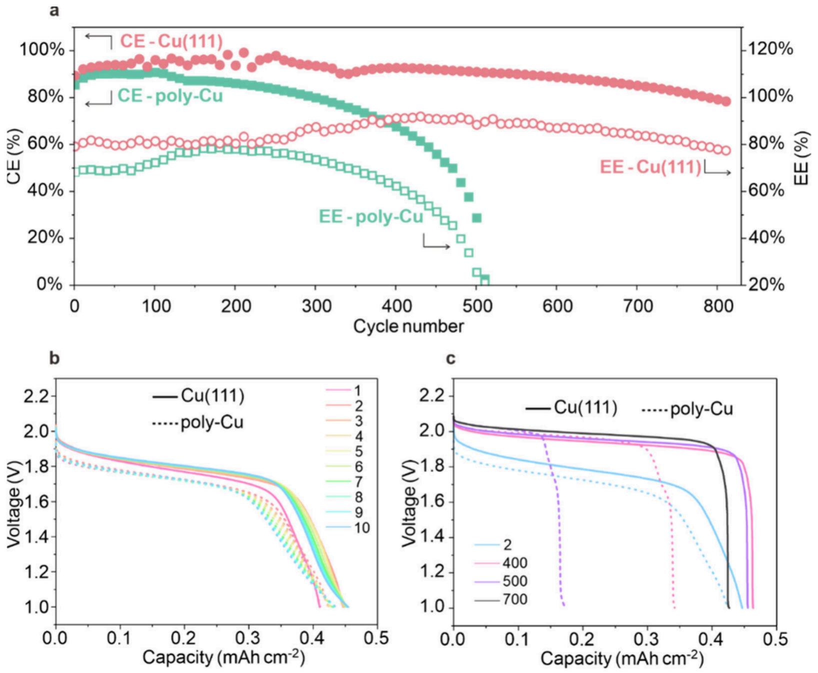

Figure 5. Full cell cycling test of a MnO_2−Zn aqueous battery with both cathode-free and anode-free electrodes. (a) Coulombic efficiency and energy efficiency of pristine copper foil and Cu(111) foil as the anode-free current collectors (electrolyte: 1 M $MnSO_4$ + 1 M $ZnSO_4$, charge at 2.2 V to 0.5 mAh cm^{-2}, then discharged at 5 mA cm^{-2} with a cutoff voltage of 1.0 V). (b) The first 10 discharge curves of Cu(111) foil (solid curve) and poly-Cu foil (dash curve) in the Mn−Zn full cell. (c) The second, 400th, 500th, and 700th discharge curves of Cu(111) foil (solid curve) and poly-Cu foil (dash curve) in a Mn−Zn full cell.

This method visually confirms the Cu(111)−Zn(0002) epitaxial relationship more robustly than powder XRD. The in-plane angle $\Delta\Phi$ of 60° (Figure 3g) at this interface achieved by dual-pole figure characterization indicates a similar atomic arrangement between Cu(111) and Zn(0002), as shown in Figure S8c.

Similarly, generating atomic arrangements for the Cu(100)/Zn(10$\bar{1}$1) interface and Cu(110)/Zn(10$\bar{1}$2) interface (Figure S8a,b, Figure 3e,f) is achievable through their pole figures (Figures 3b,c, S9, and S10). In contrast to the single-dot pattern in Cu(110)/Zn(10$\bar{1}$2) and Cu(111)/Zn(0002) systems, the Cu(100)/ Zn(10$\bar{1}$1) system exhibits a highly crystalline Cu(100) signal but two separated cyan areas of zinc, averagely perpendicular to each other for zinc. This difference arises from the rectangular symmetry of Cu(100) conflicting with the asymmetry of Zn(10$\bar{1}$1), resulting in two different zinc plating orientations. This discrepancy can lead to grain-to-grain stress, which could compromise the epitaxial relationship. These pole figure findings align precisely with SEM and reversibility observations (Figure 2a−h, p), reinforcing their accuracy. Additionally, the extensive X-ray irradiation area during pole figure measurements, surpassing 5 mm × 5 mm, suggests that these results provide reliable three-dimensional statistical evidence of uniformity at the Cu(110)/Zn(10$\bar{1}$2) and Cu(111)/Zn(0002) interfaces, confirming the consistency of epitaxial growth across large areas. Due to its superior performance in compact zinc plating, high reversibility, low nucleation overpotential, and minimal lattice misfit with the corresponding epitaxial zinc facet, Cu(111) is exceptionally well-suited for use in rechargeable zinc-ion battery applications, which will be our primary focus in subsequent battery evaluation test.

Reversibility of Zinc Anode in Symmetric Cell. The creation of large-area, high-quality single-crystal Cu(111) foil facilitates the uniform epitaxial electrodeposition of zinc. This is evident in Figure 4a, where ultraflat, millimeter-scale zinc deposition on Cu(111) is achieved after plating 1 mAh cm^{-2} of zinc. XRD analysis (Figure 4b), with a 5 mm × 5 mm irradiation area, reveals a sole significant Zn(0002) peak on Cu(111), confirming the uniformity. This large-scale flatness in zinc plating (Figure 4d), unprecedented in previous reports, contrasts with the uneven deposition on poly-Cu (Figure 4c). These findings validate the effectiveness of high-quality Cu(111) foil in achieving large-area dendrite-free zinc plating.

To evaluate the benefits of uniform zinc plating, we used symmetric cells with 5 mAh cm^{-2} predeposited Zn on Cu and cycled them at 1 mA cm^{-2} to 0.5 mAh cm^{-2}. Poly-Cu showed higher overpotential and a shorter cycle life (235 cycles) compared to Cu(111)'s 880 cycles (Figure 4e). Increasing the capacity to 5 mAh cm^{-2} at 10 mA cm^{-2} led to failure in poly-Cu after 34 cycles, whereas Cu(111) sustained over 450 cycles (Figure S12). In addition to preventing short-circuiting, dendrite-free zinc growth results in a denser zinc layer, which reduces the surface area exposed to water and thereby decreases corrosion. Linear polarization tests show that the corrosion current for zinc on Cu(111) is 0.68 mA cm^{-2}, only half of poly-Cu (1.42 mA cm^{-2}), indicating significantly reduced corrosion on Cu(111) (Figure 4f). This reduced corrosion on Cu(111) prevents the formation of a dense solid electrolyte interface on electrodeposited zinc, which, in the case of poly-Cu, leads to higher overpotentials during cycling (Figure 4e).

Full Cell Performance of MnO_2−Zn Cathode−Anode−Free Battery. To test the full cell efficacy using Cu(111) as the anode current collector, we selected the MnO_2−Zn aqueous battery due to its environmental friendliness, cost-effectiveness, mishandling tolerance, and reasonable energy density.[50−54] Using carbon felt as a cathode-free current collector and copper foil as an anode-free current collector, we compared the cycling performances of poly-Cu and Cu(111) (Figure 5).

The Cu(111) sustained 811 cycles with only 20% capacity loss, significantly outperforming poly-Cu, which lasted only 500 cycles with over 70% capacity loss (Figure 5a). This longevity with Cu(111) is a notable achievement in cathode-anode-free MnO_2−Zn batteries. The energy efficiency further highlights Cu(111)'s superiority, maintaining a stable 80% efficiency, whereas poly-Cu plummeted to 20% at the 500th cycle. This is attributed to the severe corrosion and porous plating of zinc on poly-Cu. Detailed discharge curves (Figure 5b,c) further illustrate Cu(111)'s lower overpotential and capacity loss, benefiting from the epitaxially driven compact zinc plating. Compared with poly-Cu, the higher discharge plateau in Cu(111) is attributed to less electronic resistance caused by corrosion product coating and lower electrolyte pH due to less proton consumption from corrosion. Moreover, this exceptional performance of Cu(111) compared to poly-Cu was consistently observed across multiple discharge current densities (Figure S13).

In summary, we successfully synthesized three highly orientated copper facets and comprehensively examined the epitaxial growth of zinc on various copper surfaces (Cu(100), Cu(110), Cu(111)) and on unprocessed poly-Cu using an aqueous electrolyte. The epitaxial pairings of Cu(100)/Zn($10\bar{1}1$), Cu(110)/Zn($10\bar{1}2$) and Cu(111)/Zn(0002) were verified through both practical experiments and theoretical analysis. Notably, the Cu(111) facet demonstrated the most favorable conditions for zinc diffusion and epitaxial growth, marked by the lowest energy barriers and the lowest interfacial energy. This leads to superior zinc plating qualities, exhibiting high Coulombic efficiency (99.93%), 20 mAh cm^{-2} Zn plating with no porosity, and large area of dendrite-free zinc plating. These exceptional attributes contribute to record-setting performance in rechargeable zinc aqueous batteries using a standard $ZnSO_4$ salt. The Cu(111) electrode showed remarkable cyclability, exceeding 880 cycles in half-cell configurations and achieving an unprecedented 811 cycles in MnO_2−Zn batteries with a cathode-anode-free setup. These findings offer valuable insights into the electrochemical epitaxial relationship between zinc and copper, highlighting Cu(111) as an optimal material for current collectors in rechargeable zinc batteries. The potential for large-scale application of Cu(111) in these batteries as current collectors is significant, especially considering the current rise in research and industrialization of 2D materials, promising high-quality, cost-effective solutions.

■ ASSOCIATED CONTENT

Supporting Information

The Supporting Information is available free of charge at https://pubs.acs.org/doi/10.1021/acs.nanolett.4c04535.

> Experimental details, SEM and XRD characterization comparison between poly-Cu and Cu(111), zinc morphology on Cu(111) in different electrolyte, diffusion energy barrier and interfacial energy of zinc on Cu, in situ optical cell observation, detailed pole figure illustration, and more symmetric cycling and full cell cycling results (PDF)
>
> In-situ optical cell observations of zinc electrodeposition on poly-Cu (MP4)
>
> In-situ optical cell observations of zinc electrodeposition on Cu(111) (MP4)

■ AUTHOR INFORMATION

Corresponding Author

Yi Cui − *Department of Materials Science and Engineering, Stanford University, Stanford, California 94305, United States; Department of Energy Science and Engineering, Stanford University, Stanford, California 94305, United States; Stanford Institute for Materials and Energy Sciences, SLAC National Accelerator Laboratory, Menlo Park, California 94025, United States;* orcid.org/0000-0002-6103-6352; Email: yicui@stanford.edu

Authors

Xin Xiao − *Department of Materials Science and Engineering, Stanford University, Stanford, California 94305, United States;* orcid.org/0000-0003-1098-9484

Louisa C. Greenburg − *Department of Materials Science and Engineering, Stanford University, Stanford, California 94305, United States;* orcid.org/0000-0002-0545-0081

Yuqi Li − *Department of Materials Science and Engineering, Stanford University, Stanford, California 94305, United States;* orcid.org/0000-0003-1501-1549

Menghao Yang − *Department of Chemical Engineering, Stanford University, Stanford, California 94305, United States;* orcid.org/0000-0001-7926-5113

Yan-Kai Tzeng − *Department of Physics, Stanford University, Stanford, California 94305, United States*

Chenxi Sui − *Pritzker School of Molecular Engineering, University of Chicago, Chicago, Illinois 60637, United States;* orcid.org/0000-0003-2244-8431

Yucan Peng − *Department of Materials Science and Engineering, Stanford University, Stanford, California 94305, United States*

Yecun Wu − *Department of Physics, Stanford University, Stanford, California 94305, United States;* orcid.org/0000-0001-6011-4489

Zewen Zhang − *Department of Materials Science and Engineering, Stanford University, Stanford, California 94305, United States*

Xin Gao − *Department of Materials Science and Engineering, Stanford University, Stanford, California 94305, United States*

Rong Xu − *Department of Materials Science and Engineering, Stanford University, Stanford, California 94305, United States*

Yusheng Ye − *Department of Materials Science and Engineering, Stanford University, Stanford, California 94305, United States;* orcid.org/0000-0001-9832-2478

Pu Zhang − *Department of Materials Science and Engineering, Stanford University, Stanford, California 94305, United States*

Yufei Yang − *Department of Materials Science and Engineering, Stanford University, Stanford, California 94305, United States;* orcid.org/0000-0002-3480-095X

Arturas Vailionis − *Stanford Nano Shared Facilities, Stanford University, Stanford, California 94305, United States; Department of Physics, Kaunas University of Technology, LT-51368 Kaunas, Lithuania*

Po-chun Hsu − *Pritzker School of Molecular Engineering, University of Chicago, Chicago, Illinois 60637, United States;* orcid.org/0000-0002-6509-9377

Jian Qin − *Department of Chemical Engineering, Stanford University, Stanford, California 94305, United States;* orcid.org/0000-0001-6271-068X

Complete contact information is available at:
https://pubs.acs.org/10.1021/acs.nanolett.4c04535

Author Contributions

X.X. and Y.C. conceived the initial idea. X.X. and Y.C. designed experiments. X.X. conducted experiments with the help of L.C.G., Y.L., and Y.T. M.Y. performed theoretical computation. A.V. guided the pole figure characterization. X.X. and Y.C. wrote the manuscript with input from all coauthors.

Notes

The authors declare no competing financial interest.

■ ACKNOWLEDGMENTS

This work is supported by the Aqueous Battery Consortium, an energy innovation hub under the U.S. Department of Energy, Office of Basic Energy Sciences, Division of Materials Science and Engineering. Part of this work was performed at the Stanford Nano Shared Facilities (SNSF) and Stanford Nanofabrication Facility (SNF), both supported by the National Science Foundation under award ECCS-1542152.

■ REFERENCES

(1) *2023 Energy Storage Market Outlook*; BNEF, 2023. https://about.bnef.com/blog/1h-2023-energy-storage-market-outlook/ (accessed Dec. 13, 2023).

(2) Kundu, D.; Adams, B. D.; Duffort, V.; Vajargah, S. H.; Nazar, L. F. A high-capacity and long-life aqueous rechargeable zinc battery using a metal oxide intercalation cathode. *Nat. Energy* **2016**, *1*, 16119.

(3) Pan, H. L.; Shao, Y. Y.; Yan, P. F.; Cheng, Y. W.; Han, K. S.; Nie, Z. M.; Wang, C. M.; Yang, J. H.; Li, X. L.; Bhattacharya, P.; et al. Reversible aqueous zinc/manganese oxide energy storage from conversion reactions. *Nat. Energy* **2016**, *1*, 16039.

(4) Wang, F.; Borodin, O.; Gao, T.; Fan, X. L.; Sun, W.; Han, F. D.; Faraone, A.; Dura, J. A.; Xu, K.; Wang, C. S. Highly reversible zinc metal anode for aqueous batteries. *Nat. Mater.* **2018**, *17* (6), 543−549.

(5) Wang, L. J.; Zhang, Y.; Hu, H. L.; Shi, H. Y.; Song, Y.; Guo, D.; Liu, X. X.; Sun, X. Q. A $Zn(ClO_4)_2$ electrolyte enabling long-life zinc metal electrodes for rechargeable aqueous zinc batteries. *ACS Appl. Mater. Interfaces* **2019**, *11* (45), 42000−42005.

(6) Li, G. D.; Chen, W.; Zhang, H.; Gong, Y. J.; Shi, F. F.; Wang, J. Y.; Zhang, R. F.; Chen, G. X.; Jin, Y.; Wu, T.; et al. Membrane-free Zn/MnO_2 flow battery for large-scale energy storage. *Adv. Energy Mater.* **2020**, *10* (9), 1902085.

(7) Winter, M.; Barnett, B.; Xu, K. Before Li ion batteries. *Chem. Rev.* **2018**, *118* (23), 11433−11456.

(8) Yaroshevsky, A. A. Abundances of chemical elements in the Earth's crust. *Geochem. Int.* **2006**, *44* (1), 48−55.

(9) Yue, J. S.; Chen, S.; Yang, J. J.; Li, S. Q.; Tan, G. Q.; Zhao, R.; Wu, C.; Bai, Y. Multi-ion engineering strategies toward high performance aqueous zinc-based batteries. *Adv. Mater.* **2024**, *36*, 2304040.

(10) Parker, J. F.; Chervin, C. N.; Nelson, E. S.; Rolison, D. R.; Long, J. W. Wiring zinc in three dimensions re-writes battery performance-dendrite-free cycling. *Energy Environ. Sci.* **2014**, *7* (3), 1117−1124.

(11) Lv, W.; Shen, Z. L.; Li, X. D.; Meng, J. W.; Yang, W. J.; Ding, F.; Ju, X.; Ye, F.; Li, Y. M.; Lyu, X.; et al. Discovering cathodic biocompatibility for aqueous Zn-MnO_2 battery: An integrating biomass carbon strategy. *Nano-Micro Lett.* **2024**, *16* (1), 109.

(12) Ming, F. W.; Zhu, Y. P.; Huang, G.; Emwas, A. H.; Liang, H. F.; Cui, Y.; Alshareef, H. N. Co-solvent electrolyte engineering for stable anode-free zinc metal batteries. *J. Am. Chem. Soc.* **2022**, *144* (16), 7160−7170.

(13) Yang, C. Y.; Xia, J. L.; Cui, C. Y.; Pollard, T. P.; Vatamanu, J.; Faraone, A.; Dura, J. A.; Tyagi, M.; Kattan, A.; Thimsen, E.; et al. All-temperature zinc batteries with high-entropy aqueous electrolyte. *Nat. Sustain.* **2023**, *6* (3), 325−335.

(14) Wang, Y. B.; Li, Q.; Hong, H.; Yang, S.; Zhang, R.; Wang, X. Q.; Jin, X.; Xiong, B.; Bai, S. C.; Zhi, C. Y. Lean-water hydrogel electrolyte for zinc ion batteries. *Nat. Commun.* **2023**, *14* (1), 3890.

(15) Lv, W.; Meng, J. W.; Li, X. D.; Xu, C.; Yang, W. J.; Duan, S. Z.; Li, Y. M.; Ju, X.; Yuan, R. S.; Tian, Y.; et al. et al. Boosting zinc storage in potassium-birnessite via organic-inorganic electrolyte strategy with slight N-methyl-2-pyrrolidone additive. *Energy Stor. Mater.* **2023**, *54*, 784−793.

(16) Guo, J.; Ming, J.; Lei, Y. J.; Zhang, W. L.; Xia, C.; Cui, Y.; Alshareef, H. N. Artificial solid electrolyte interphase for suppressing surface reactions and cathode dissolution in aqueous zinc ion batteries. *ACS Energy Lett.* **2019**, *4* (12), 2776−2781.

(17) Kang, L. T.; Cui, M. W.; Jiang, F. Y.; Gao, Y. F.; Luo, H. J.; Liu, J. J.; Liang, W.; Zhi, C. Y. Nanoporous $CaCO_3$ coatings enabled uniform zn stripping/plating for long-life zinc rechargeable aqueous batteries. *Adv. Energy Mater.* **2018**, *8* (25), 1801090.

(18) Zhang, Q.; Luan, J. Y.; Tang, Y. G.; Ji, X. B.; Wang, H. Y. Interfacial design of dendrite-free zinc anodes for aqueous zinc-ion batteries. *Angew. Chem., Int. Ed.* **2020**, *59* (32), 13180−13191.

(19) Lv, W.; Meng, J. W.; Li, Y. M.; Yang, W. J.; Tian, Y. L.; Lyu, X. F.; Duan, C. W.; Ma, X. L.; Wu, Y. Inexpensive and eco-friendly nanostructured birnessite-type δ-MnO_2: A design strategy from oxygen defect engineering and K^+ pre-intercalation. *Nano Energy* **2022**, *98*, 107274.

(20) Zhang, Q.; Ma, Y. L.; Lu, Y.; Li, L.; Wan, F.; Zhang, K.; Chen, J. Modulating electrolyte structure for ultralow temperature aqueous zinc batteries. *Nat. Commun.* **2020**, *11* (1), 4463.

(21) Chen, S. G.; Lan, R.; Humphreys, J.; Tao, S. W. Salt-concentrated acetate electrolytes for a high voltage aqueous Zn/MnO_2 battery. *Energy Stor. Mater.* **2020**, *28*, 205−215.

(22) Dong, D. J.; Wang, T. R.; Sun, Y.; Fan, J.; Lu, Y. C. Hydrotropic solubilization of zinc acetates for sustainable aqueous battery electrolytes. *Nat. Sustain.* **2023**, *6*, 1474−1484.

(23) Han, S. D.; Rajput, N. N.; Qu, X. H.; Pan, B. F.; He, M. N.; Ferrandon, M. S.; Liao, C.; Persson, K. A.; Burrell, A. K. Origin of electrochemical, structural, and transport properties in nonaqueous zinc electrolytes. *ACS Appl. Mater. Interfaces* **2016**, *8* (5), 3021−3031.

(24) Naveed, A.; Yang, H. J.; Yang, J.; Nuli, Y. N.; Wang, J. L. Highly reversible and rechargeable safe zn batteries based on a triethyl phosphate electrolyte. *Angew. Chem., Int. Ed.* **2019**, *58* (9), 2760−2764.

(25) Zhang, N.; Cheng, F. Y.; Liu, Y. C.; Zhao, Q.; Lei, K. X.; Chen, C. C.; Liu, X. S.; Chen, J. Cation-deficient spinel $ZnMn_2O_4$ cathode in $Zn(CF_3SO_3)2$ electrolyte for rechargeable aqueous Zn-ion battery. *J. Am. Chem. Soc.* **2016**, *138* (39), 12894−12901.

(26) Wang, N.; Dong, X. L.; Wang, B. L.; Guo, Z. W.; Wang, Z.; Wang, R. H.; Qiu, X.; Wang, Y. G. Zinc-organic battery with a wide operation-temperature window from-70 to 150 °C. *Angew. Chem., Int. Ed.* **2020**, *59* (34), 14577−14583.

(27) Wang, N.; Yang, Y.; Qiu, X.; Dong, X. L.; Wang, Y. G.; Xia, Y. Y. Stabilized rechargeable aqueous zinc batteries using ethylene glycol as water blocker. *ChemSusChem* **2020**, *13* (20), 5556−5564.

(28) Kao-ian, W.; Nguyen, M. T.; Yonezawa, T.; Pornprasertsuk, R.; Qin, J.; Siswamogsatham, S.; Kheawhom, S. Highly stable rechargeable zinc-ion battery using dimethyl sulfoxide electrolyte. *Mater. Today Energy* **2021**, *21*, 100738.

(29) Zhao, Z. M.; Zhao, J. W.; Hu, Z. L.; Li, J. D.; Li, J. J.; Zhang, Y. J.; Wang, C.; Cui, G. L. Long-life and deeply rechargeable aqueous Zn anodes enabled by a multifunctional brightener-inspired interphase. *Energy Environ. Sci.* **2019**, *12* (6), 1938−1949.

(30) Lee, B. S.; Cui, S.; Xing, X.; Liu, H. D.; Yue, X. J.; Petrova, V.; Lim, H. D.; Chen, R. K.; Liu, P. Dendrite suppression membranes for

rechargeable zinc batteries. *ACS Appl. Mater. Interfaces* **2018**, *10* (45), 38928−38935.

(31) Zhao, K. N.; Wang, C. X.; Yu, Y. H.; Yan, M. Y.; Wei, Q. L.; He, P.; Dong, Y. F.; Zhang, Z. Y.; Wang, X. D.; Mai, L. Q. Ultrathin surface coating enables stabilized zinc metal anode. *Adv. Mater. Interfaces* **2018**, *5* (16), 1800848.

(32) Zeng, X. M.; Zhao, J.; Wan, Z. W.; Jiang, W.; Ling, M.; Yan, L. J.; Liang, C. D. Controllably electrodepositing ZIF-8 protective layer for highly reversible zinc anode with ultralong lifespan. *J. Phys. Chem. Lett.* **2021**, *12* (37), 9055−9059.

(33) Yang, Q.; Liang, G.; Guo, Y.; Liu, Z.; Yan, B.; Wang, D.; Huang, Z.; Li, X.; Fan, J.; Zhi, C. Do zinc dendrites exist in neutral zinc batteries: A developed electrohealing strategy to in situ rescue in-service batteries. *Adv. Mater.* **2019**, *31* (43), 1903778.

(34) Zheng, J. X.; Zhao, Q.; Tang, T.; Yin, J. F.; Quilty, C. D.; Renderos, G. D.; Liu, X. T.; Deng, Y.; Wang, L.; Bock, D. C.; et al. Reversible epitaxial electrodeposition of metals in battery anodes. *Science* **2019**, *366* (6465), 645−648.

(35) Xie, C. L.; Ji, H. M.; Zhang, Q.; Yang, Z. F.; Hu, C.; Ji, X. B.; Tang, Y. G.; Wang, H. Y. High-index zinc facet exposure induced by preferentially orientated substrate for dendrite-free zinc anode. *Adv. Energy Mater.* **2023**, *13* (3), 2203203.

(36) Liu, Z. P.; Guo, Z. K.; Fan, L. S.; Zhao, C. Y.; Chen, A. S.; Wang, M.; Li, M.; Lu, X. Y.; Zhang, J. C.; Zhang, Y.; et al. Construct robust epitaxial growth of (101) textured zinc metal anode for long life and high capacity in mild aqueous zinc-ion batteries. *Adv. Mater.* **2024**, *36*, 2305988.

(37) Wang, M.; Wang, W.; Meng, Y.; Xu, Y.; Sun, J.; Yuan, Y.; Chuai, M.; Chen, N.; Zheng, X.; Luo, R.; Xu, K.; Chen, W. Crystal facet correlated Zn growth on Cu for aqueous Zn metal batteries. *Energy Stor. Mater.* **2023**, *56*, 424−431.

(38) Hao, Z.; Zhang, Y.; Hao, Z.; Li, G.; Lu, Y.; Jin, S.; Yang, G.; Zhang, S.; Yan, Z.; Zhao, Q.; Chen, J. Metal anodes with ultrahigh reversibility enabled by the closest packing crystallography for sustainable batteries. *Adv. Mater.* **2023**, *35* (9), 2209985.

(39) Su, Y.; Chen, B.; Sun, Y.; Xue, Z.; Zou, Y.; Yang, D.; Sun, L.; Yang, X.; Li, C.; Yang, Y.; Song, X.; Guo, W.; Dou, S.; Chao, D.; Liu, Z.; Sun, J. Rationalized electroepitaxy toward scalable single-crystal Zn anodes. *Adv. Mater.* **2023**, *35* (28), 2301410.

(40) Yi, Z.; Liu, J.; Tan, S.; Sang, Z.; Mao, J.; Yin, L.; Liu, X.; Wang, L.; Hou, F.; Dou, S. X.; Cheng, H.-M.; Liang, J. An ultrahigh rate and stable zinc anode by facet-matching-induced dendrite regulation. *Adv. Mater.* **2022**, *34* (37), 2203835.

(41) Li, Y.; Sun, L.; Chang, Z.; Liu, H.; Wang, Y.; Liang, Y.; Chen, B.; Ding, Q.; Zhao, Z.; Wang, R.; Wei, Y.; Peng, H.; Lin, L.; Liu, Z. Large single-crystal Cu foils with high-index facets by strain-engineered anomalous grain growth. *Adv. Mater.* **2020**, *32* (29), 2002034.

(42) Zhang, X. P.; Han, J.; Plombon, J. J.; Sutton, A. P.; Srolovitz, D. J.; Boland, J. J. Nanocrystalline copper films are never flat. *Science* **2017**, *357* (6349), 397−399.

(43) Wang, H.; Xu, X. Z.; Li, J. Y.; Lin, L.; Sun, L. Z.; Sun, X.; Zhao, S. L.; Tan, C. W.; Chen, C.; Dang, W. H.; et al. Surface monocrystallization of copper foil for fast growth of large single-crystal graphene under free molecular flow. *Adv. Mater.* **2016**, *28* (40), 8968−8974.

(44) *METX toolbox_EBSD*; MTEX, 2024. https://mtex-toolbox.github.io/ (accessed Nov 26, 2024).

(45) Xiao, X.; Zhang, Z. W.; Wu, Y. C.; Xu, J. W.; Gao, X.; Xu, R.; Huang, W. X.; Ye, Y. S.; Oyakhire, S. T.; Zhang, P.; et al. Ultrahigh-loading manganese-based electrodes for aqueous batteries via polymorph tuning. *Adv. Mater.* **2023**, *35* (33), 2211555.

(46) Ma, L.; Schroeder, M. A.; Borodin, O.; Pollard, T. P.; Ding, M. S.; Wang, C. S.; Xu, K. Realizing high zinc reversibility in rechargeable batteries. *Nat. Energy* **2020**, *5* (10), 743−749.

(47) Adams, B. D.; Zheng, J. M.; Ren, X. D.; Xu, W.; Zhang, J. G. Accurate determination of coulombic efficiency for lithium metal anodes and lithium metal batteries. *Adv. Energy Mater.* **2018**, *8* (7), 1702097.

(48) Aurbach, D.; Youngman, O.; Gofer, Y.; Meitav, A. The electrochemical-behavior of 1,3-dioxolane-$LiClO_4$ solutions.1. Uncontaminated solutions. *Electrochim. Acta* **1990**, *35* (3), 625−638.

(49) Yu, Z.; Wang, H. S.; Kong, X.; Huang, W.; Tsao, Y. C.; Mackanic, D. G.; Wang, K. C.; Wang, X. C.; Huang, W. X.; Choudhury, S.; et al. Molecular design for electrolyte solvents enabling energy-dense and long-cycling lithium metal batteries. *Nat. Energy* **2020**, *5* (7), 526−533.

(50) Sun, W.; Wang, F.; Hou, S. Y.; Yang, C. Y.; Fan, X. L.; Ma, Z. H.; Gao, T.; Han, F. D.; Hu, R. Z.; Zhu, M.; et al. Zn/MnO_2 battery chemistry with H^+ and Zn^{2+} coinsertion. *J. Am. Chem. Soc.* **2017**, *139* (29), 9775−9778.

(51) Chao, D. L.; Zhou, W. H.; Xie, F. X.; Ye, C.; Li, H.; Jaroniec, M.; Qiao, S. Z. Roadmap for advanced aqueous batteries: From design of materials to applications. *Sci. Adv.* **2020**, *6* (21), No. eaba4098.

(52) Chao, D. L.; Zhou, W. H.; Ye, C.; Zhang, Q. H.; Chen, Y. G.; Gu, L.; Davey, K.; Qiao, S. Z. An electrolytic Zn-MnO_2 battery for high-voltage and scalable energy storage. *Angew. Chem., Int. Ed.* **2019**, *58* (23), 7823−7828.

(53) Gao, X. Y.; Zhang, H. Z.; Liu, X. Q.; Lu, X. H. Flexible Zn-ion batteries based on manganese oxides: Progress and prospect. *Carbon Energy* **2020**, *2* (3), 387−407.

(54) Chang, H. J.; Rodríguez-Pérez, I. A.; Fayette, M.; Canfield, N. L.; Pan, H. L.; Choi, D.; Li, X. L.; Reed, D. Effects of water-based binders on electrochemical performance of manganese dioxide cathode in mild aqueous zinc batteries. *Carbon Energy* **2021**, *3* (3), 473−481.